PHYSICAL REVIEW A **89**, 033610 (2014)

Splitting bright matter-wave solitons on narrow potential barriers: Quantum to classical transition and applications to interferometry

J. L. Helm,[1] S. J. Rooney,[2] Christoph Weiss,[1] and S. A. Gardiner[1]
[1]*Joint Quantum Centre Durham-Newcastle, Department of Physics, Durham University, Durham DH1 3LE, United Kingdom*
[2]*Jack Dodd Centre for Quantum Technology, Department of Physics, University of Otago, Dunedin, New Zealand*

(Received 28 January 2014; published 10 March 2014)

We study bright solitons in the Gross-Pitaevskii equation as they are split and recombined in a low-energy system. We present analytic results determining the general region in which a soliton may not be split on a potential barrier and confirm these results numerically. Furthermore, we analyze the energetic regimes where quantum fluctuations in the initial center-of-mass position and momentum become influential on the outcome of soliton splitting and recombination events. We then use the results of this analysis to determine a parameter regime where soliton interferometry is practicable.

DOI: 10.1103/PhysRevA.89.033610 PACS number(s): 03.75.Lm, 05.45.Yv, 67.85.De

I. INTRODUCTION

Atomic Bose-Einstein condensates (BECs) with attractive interatomic interactions are capable of supporting solitonlike dynamical excitations referred to as bright solitary matter waves [1–5]. These excitations are solitonlike in the sense that they propagate without dispersion [6], are robust to collisions with both other bright solitary matter waves and slowly varying external potentials [7,8], and have center-of-mass trajectories which are well described by effective particle models [9–11]. They derive these solitonlike properties from their analogousness to the bright soliton solutions of the focusing nonlinear Schrödinger equation (NLSE) [12–16], to which the mean-field description of an atomic BEC reduces in an effectively unconfined, quasi-one-dimensional (quasi-1D) limit. Although the quasi-1D limit is experimentally challenging for attractive condensates [17], bright solitary matter-wave dynamics remain highly solitonlike outside this limit [3,8]. Consequently, bright solitary matter waves present an intriguing candidate system for future interferometric devices [2,8,18–25].

The collision of a bright solitary wave with a narrow potential barrier is a good candidate for a mechanism for the creation of coherent localized condensates, much as a beam splitter coherently splits a light beam in an optical interferometer. This mechanism has been investigated extensively in the quasi-1D, mean-field description of an atomic BEC [18,26–35], and sufficiently fast collisions with potential barriers have been shown to lead to the desired beam-splitting effect [30,31]. Similarly, the dynamics of solitons has been studied in nonlinear optics in an inhomogeneous array of discrete wave guides. In this system the inhomogeneity facilitates reflection, splitting, or capture of the soliton [36–38]. This is equivalent, in the continuum limit of an infinite number of wave guides, to splitting a soliton in the Gross-Pitaevskii equation (GPE) at a δ-function potential barrier [36]. In the optics community this phenomenon has been called the "optical axe" [16]. Incomplete or bound-state splitting has been considered in the context of soliton molecule formation [22], within a mean-field description, and also in the context of many-body quantum mechanical descriptions: In the latter it has been demonstrated that macroscopic quantum superpositions of solitary waves could be created, offering intriguing possibilities for future atom interferometry experiments [20,21].

A related work [23] considered an interferometer using a narrow potential barrier as a beam splitter for harmonically trapped solitary waves, based on the particular configuration of a recent experiment [39]. In particular, this work demonstrated that such a potential barrier can also be used to recombine solitary waves, by arranging for them to collide at the location of the barrier. The dynamics of these collisions were further explained in Ref. [18]. In such collisions, the relative norms of the two outgoing solitary waves was shown to be governed by the phase difference Δ between the incoming ones. In the mean-field description the relative norms of the outgoing waves exhibit enhanced sensitivity to small variations in the phase Δ; however, a simulation of the same system including quantum noise via the truncated Wigner method [40] showed increased number fluctuations that ultimately negated this enhancement [23].

In the current work, our first result will be to carefully explore the spectrum of splitting behaviors which these systems can exhibit. It has been established that quantum superpositions, in the form of "NOON states" or "Schrödinger cat states," can be created when the energy associated with the splitting event is particularly low [20,41]. Here we wish to determine the location of the boundary between this quantum behavior and more classical behavior, which will determine where interferometry is a more practical goal. We will also present a rigorous determination of the phase shift accrued between the resulting solitons after a splitting event, based on the work presented in Ref. [30]. Our second major result will be to more thoroughly outline two different geometries which might be employed for soliton interferometry and again delineate energetic regimes where these implementations are practicable.

The current publication is presented as follows. In Sec. II we formally introduce the 3D mean-field Hamiltonian of the system, the reduced 1D Hamiltonian, and the associated dynamic equation (the GPE). In Sec. III we outline the energetic regimes of soliton splitting in the GPE, presenting analytic results in Sec. III B and comparing these results to numerical simulations in Sec. III C. We then establish the quantum uncertainties associated with the harmonically trapped system (Sec. III E). These uncertainties are used to determine a sensitivity measure of the equal splitting case (Sec. III F 2) and the distributions of the transmission after the addition of quantum fluctuations (Sec. III F 3). The last part of this section, Sec. III G, presents a derivation of the split-induced phase shift. The final results section (Sec. IV) outlines how these results might be implemented to perform Mach-Zehnder interferometry in a torus (Sec. IV B) and Mach-Zehnder interferometry in a harmonic trap (Sec. IV C). In these sections we delimit regimes where these forms of interferometry are experimentally viable in terms of the collisional energy of the system. We also outline the effects of quantum uncertainty on the harmonically trapped interferometry case (Secs. IV C 3 and IV C 4).

II. PHYSICAL SYSTEM

We begin with the 3D N-particle mean-field energy Hamiltonian $\mathcal{H}[\psi]$ for a Bose field, defined as [42]

$$\mathcal{H}[\Psi] = \int d\mathbf{r}\left[\frac{\hbar^2}{2m}|\nabla\Psi(\mathbf{r})|^2 + V_{\rm ext}(\mathbf{r})|\Psi(\mathbf{r})|^2 - \frac{2\pi N|a_s|\hbar^2}{m}|\Psi(\mathbf{r})|^4\right]. \tag{1}$$

Here N, m, and a_s are the atom number, mass, and s-wave scattering length, respectively. A δ function contact potential is assumed. For attractive interatomic interactions $a_s < 0$. The wave function, Ψ, is normalized to 1. The potential $V_{\rm ext}(\mathbf{r})$ is composed of both the trapping potentials and any external potentials used to construct narrow barriers used for splitting the soliton. We model this potential as

$$V_{\rm ext}(\mathbf{r}) = E_{\rm B}\,\mathrm{e}^{-2x^2/x_r^2} + \frac{m}{2}\left[\omega_{\rm T}^2x^2 + \omega_r(y^2+z^2)\right]. \tag{2}$$

The first term describes the narrow splitting barrier and can be generated by an off-resonant Gaussian light sheet [4] perpendicular to the x direction with $1/e^2$ radius x_r in the x direction, with peak beam strength $E_{\rm B}$. The second term denotes a standard magnetic harmonic confinement which we take to be a cylindrically symmetric wave guide; such a configuration is approximately achieved in an atomic wave-guide trap.

By increasing the radial trapping we can reach a quasi-1D regime, as defined in detail in Ref. [17], where the radial trapping is tight but remains 3D [$a_s \ll (\hbar/m\omega_r)^{1/2}$]. In this regime we can separate the radial and axial dynamics with the ansatz $\Psi(\mathbf{r}) = \Psi_{\rm 1D}(x)(m\omega_r/\pi\hbar)^{1/2}\exp(-m\omega_r[y^2+z^2]/2\hbar)$. After factoring out global phases associated with the radial harmonic ground-state energies, this yields both the quasi-1D classical field Hamiltonian [42],

$$\mathcal{H}_{\rm 1D}[\Psi_{\rm 1D}] = \int dx\left[\frac{\hbar^2}{2m}\left|\frac{\partial}{\partial x}\Psi_{\rm 1D}(x)\right|^2 + V_{\rm ext}(x)|\Psi_{\rm 1D}(x)|^2 - \frac{gN}{2}|\Psi_{\rm 1D}(x)|^4\right], \tag{3}$$

and its associated quasi-1D GPE [42],

$$i\hbar\frac{\partial\Psi_{\rm 1D}(x)}{\partial t} = \left[-\frac{\hbar^2}{2m}\frac{\partial^2}{\partial x^2} + V_{\rm ext}(x) - gN|\Psi_{\rm 1D}(x)|^2\right]\Psi_{\rm 1D}(x). \tag{4}$$

The nonlinearity is quantified by $g = 2\hbar\omega_r|a_s|$. If we take $V_{\rm ext} = 0$ then this equation reduces to the NLSE. We also consider a toroidal ring trap [43–45] by setting $\omega_{\rm T} = 0$ and introducing periodicity in x.

Working in soliton units—position units of $\hbar^2/mgN$, time units of $\hbar^3/mg^2N^2$, and energy units of $mg^2N^2/\hbar^2$ [17]—yields the dimensionless, quasi-1D GPE[1]

$$i\frac{\partial\psi(x)}{\partial t} = \left[-\frac{1}{2}\frac{\partial^2}{\partial x^2} + \frac{q}{\sigma_{\rm b}\sqrt{2\pi}}e^{-x^2/2\sigma^2} + \frac{\omega_x^2x^2}{2} - |\psi(x)|^2\right]\psi(x), \tag{5}$$

where the dimensionless wave function is $\psi = \hbar\Psi_{\rm 1D}/\sqrt{mgN}$, the barrier width is characterized by $\sigma_{\rm b}$ (the dimensionless form of half the $1/e^2$ radius), and the barrier strength is given by

$$q = \sqrt{\frac{\pi}{2}}\frac{E_{\rm B}x_r}{gN}. \tag{6}$$

III. SOLITON SPLITTING

A. Overview

In this section we probe the transition from low- to high-energy soliton splitting. We quantify the energy by the velocity of the soliton at the point of collision with the barrier, denoted as v for an untrapped system, where the velocity is brought about by an imprinted phase on the initial condition, or v_0 for the axially trapped system, where the velocity is a result of the axial trapping ω_x being greater than zero and an initial offset x_0 in the initial condition. This offset separates the soliton from the point where the soliton is split by the barrier at $x = 0$.

We take $v, v_0 \gtrsim 1.0$ to be the high-energy regime and $v, v_0 \lesssim 0.25$ to be the low-energy regime [41]. As such, the transitional energy regime lies within the $0.25 \leqslant v, v_0 \leqslant 1$ velocity range. We justify the lower bound of this regime by considering classical descriptions of the kinetic and ground-state energies of the system. We also show that these arguments describe a process which is analogous to the quantum mechanical transition from product state wave functions (where, after scattering the transmitted or reflected portions of the wave function can range continuously between zero and full transmission or reflection) to bimodal systems (where the soliton is either reflected by or transmitted through the barrier, but never split).[2]

B. Analysis of classical soliton splitting

We explain the transition between high- and low-energy dynamics by comparing the incoming collisional kinetic

---

[1] It should be noted that in the very low N limit this rescaling takes a slightly different form, with N replaced by $N-1$. This rescaling is used in Ref. [46].

[2] It should be noted that even in the high-energy regime we cannot make a soliton of arbitrary size by simply scattering a larger soliton off a barrier. The scattered portion of the wave function may be too small to form a soliton and must be considered radiation [30].

energy E_{K} and the energy required to split the soliton E_{S}. First, rescaling the quasi-1D Hamiltonian [Eq. (3)] into soliton units with $\omega_{\mathrm{T}} = 0$ gives

$$\mathrm{H}_{\mathrm{1D}}[\psi] = \int dx \left[\frac{1}{2} \left| \frac{\partial}{\partial x} \psi(x) \right|^2 - \frac{1}{2} |\psi(x)|^4 \right]. \tag{7}$$

We then substitute the 1D soliton solution,

$$\psi_0 = \frac{1}{2} \mathrm{sech}\left(\frac{x - x_0}{2} \right) e^{ivx}, \tag{8}$$

into our Hamiltonian, with $v = 0$, and obtain both the per-particle soliton ground-state energy ($\mathrm{H}_{\mathrm{1D}}[\psi_0] = -1/24$) and N-particle soliton ground-state energy [$E_{\mathrm{G}}(N) = -N/24$]. We then consider an n-particle soliton which is spatially well separated from the rest of the condensate and any potentials. Failure to satisfy this separation assumption may result in a bound state, and further contributions to the ground-state energy will arise. The effects of such bound states is discussed later. Assuming that the whole condensate contains a total of N particles, we see that the spatially separated soliton's contribution to the total energy is

$$E_{\mathrm{G}}(n) = -\frac{n}{24} \left(\frac{n}{N} \right)^2. \tag{9}$$

We reach this conclusion by rescaling the n-particle soliton ground-state energy $E_{\mathrm{G}}(n)$ into N-particle soliton units. This is equivalent to multiplying by $(n/N)^2$. By constructing the energy difference E_{S}, we can easily see that the energy required to split the soliton is

$$\begin{aligned} E_{\mathrm{S}} &= E_{\mathrm{G}}(N-n) + E_{\mathrm{G}}(n) - E_{\mathrm{G}}(N) \\ &= 3|E_{\mathrm{G}}(N)| \left(1 - \frac{n}{N} \right) \frac{n}{N}. \end{aligned} \tag{10}$$

We can now recast this result in terms of the transmission, T_+:

$$T_+ = \int_0^\infty |\psi|^2 dx = \frac{n}{N}, \tag{11}$$

yielding

$$E_{\mathrm{S}} = \tfrac{1}{8} T_+ (1 - T_+) N. \tag{12}$$

Next, we describe the classical particle energy of an N-particle soliton moving at velocity v:

$$E_{\mathrm{K}} = \frac{v^2 N}{2}. \tag{13}$$

We can now see that, for splitting to occur, we must satisfy $E_{\mathrm{K}} > E_{\mathrm{S}}$ and so

$$|v| > \tfrac{1}{2} \sqrt{T_+ (1 - T_+)}. \tag{14}$$

This inequality describes the high-energy regime in that parameters which do not satisfy it are only available in the low-energy regime. If we consider the functional form of our inequality we see that $\sqrt{T_+(1 - T_+)}$ is maximal for $T_+ = 0.5$, at which value we have $|v| > 0.25$. As such, the first state to become inaccessible is the equal splitting case, which cannot be accessed for $|v| < 0.25$. Equivalently, we must satisfy $E_{\mathrm{K}}/E_{\mathrm{S}} > 0.75$ [Eq. (10)]. This is consistent with results described in Ref. [41].

As noted above, splitting the soliton reduces the amount of kinetic energy available to the solitons. In the high-energy regime, this reduction is negligible and the solitons are capable of becoming well separated from the barrier, and one another, after the split occurs. At lower energies this is not always the case. As less and less energy is available to the resulting solitons, their outgoing velocities are notably reduced, and eventually the solitons become trapped at the barrier. The effect of the harmonic trap enhances this effect, as the outgoing velocity determines the maximal separation which the resulting solitons can achieve. This phenomenon is shown in Fig. 1 and is discussed in the next section.

C. Numerical analysis of classical soliton splitting

We numerically verify these results by evolving the initial condition described by Eq. (8) according to the dynamics of Eq. (5). We perform two types of evolution. For the first type we set $\omega_x = 0$ and perform integrations over a range of v and q. These calculations allow us to consider the behavior of the untrapped, true soliton to which the above analytic results apply exactly. Figures 1(a)–1(c) show the results of these simulations. For the second type of simulation we set the initial velocity $v = 0$ and integrate over a range of ω_x and q. By keeping the initial offset constant at $x_0 = -L/4$, where the numerical algorithm has spatial domain $-L/2 < x \leqslant L/2$, we are able to use ω_x to select a collisional velocity $v_0 = \omega_x x_0$. This allows us to more accurately describe the behavior we would see in an experiment where the soliton is accelerated by an axial harmonic trap. Figures 1(d)–1(f) show the results of these equations.

For all simulations the barrier is situated at the trap minimum (specifically $x = 0$) and we set the barrier width to $\sigma_{\mathrm{b}} = 0.2$. Barrier potentials of finite width and height have some limitations in the extremely high velocity regime in that if the peak energy of the barrier is not notably higher than the kinetic energy of the soliton, then the soliton classically passes over the barrier and no splitting occurs [18]. This restricts the width of the barrier in a given energy regime by requiring that the barrier be narrow enough to constitute a quickly varying potential when compared to the incoming velocity of the soliton. The energy regimes we consider in the current work are compatible with a barrier width of $\sigma_{\mathrm{b}} \lesssim 0.2$. A broader discussion of the effect of finite width (for a Rosen-Morse, i.e., sech^2 potential barrier) is presented in Ref. [32].

Figure 1(a) displays a broad scan of the q,v parameter space. At higher velocities ($v > 0.25$) we see that a continuous range of transmissions is accessible. At lower velocities this is not the case, and for $v \lesssim 0.1$ we see that we are effectively left with only full transmission and full reflection as accessible final states.

We have displayed two sets of curves of constant transmission on Fig. 1(a): solid (red) and dashed (gray). The solid (red) curves are isolines of constant transmission $T_+ = 0.1, 0.2, \ldots, 1.0$ taken from the color map itself. At higher values of v these curves are well separated, illustrating that we can access the full range of transmissions by selecting q and v accordingly. As v decreases these curves begin to converge.

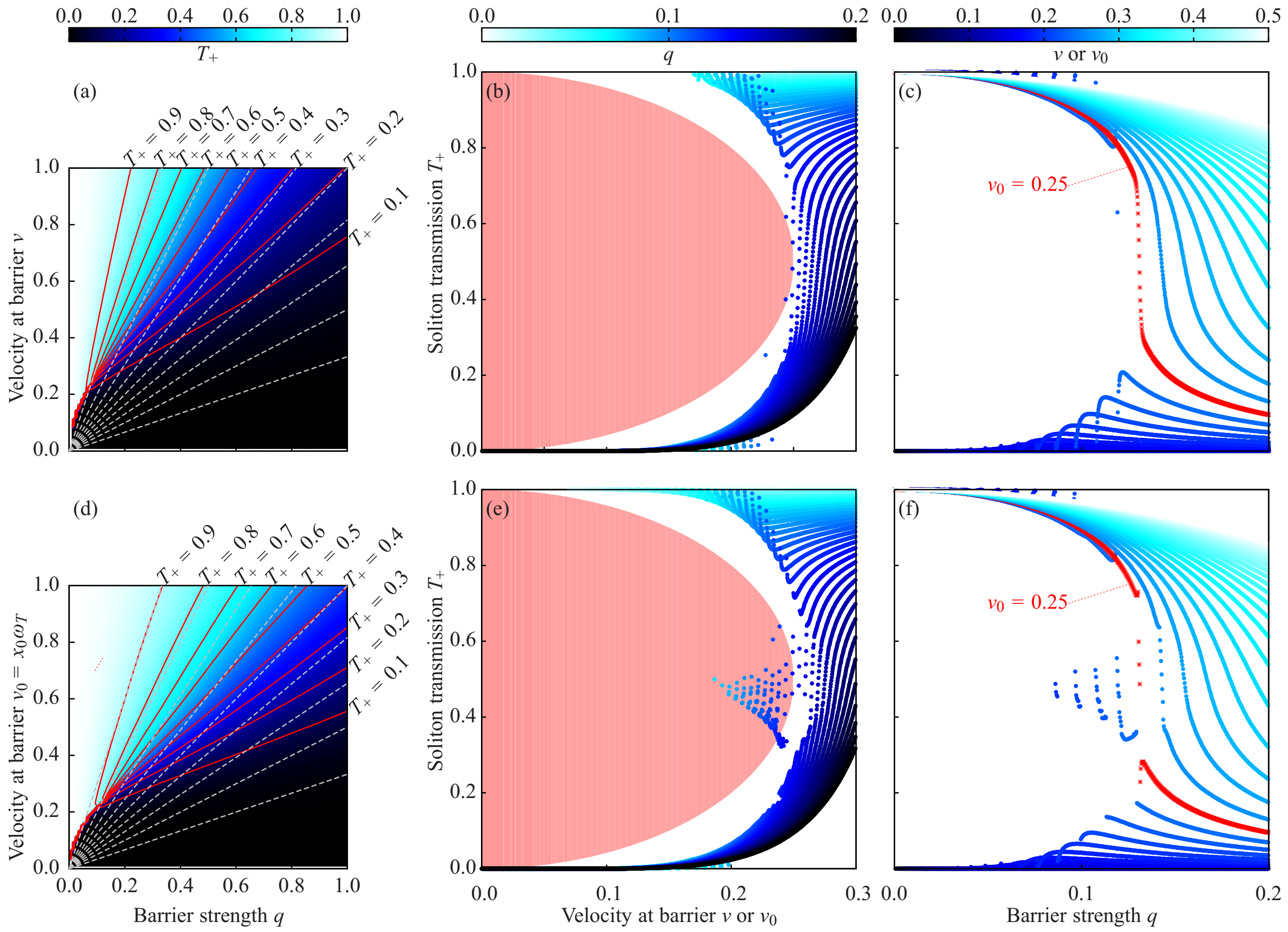

FIG. 1. (Color online) Numerical results of splitting a soliton traveling at velocity v (a)–(c) or v_0 (d)–(f) at a Gaussian barrier of strength q and width $\sigma = 0.2$. (a),(d) Color maps of transmission as a function of q and v or v_0. The solid (red) curves are isolines of constant transmission T_+ obtained from the numerics, while the dashed (gray) curves are theoretical predictions of transmission T_q^s in the linear case over the same range. (b),(e) Curves of transmission as a function of collisional velocity v or v_0 for various barrier strengths q. The shaded (red) region shows energetically disallowed splitting events. (c),(f) Curves of transmission as a function of barrier strength q for various values of v or v_0. The labeled (red) curve, for which $v,v_0 = 0.25$ indicates the classical, untrapped lower-energy bound on the region where a continuous range of transmission is accessible.

The convergence of isocurves signifies that the splitting state associated with the curves has become disallowed.

We derived the second set of curves in Fig. 1, the dashed (gray) curves, from analysis presented in Ref. [30]. The analysis states that for a δ-function barrier in the regime where both the mean-field interpretation is valid and the velocity is high the transmission is given by

$$T_q^s(v) = \lim_{t\to\infty} \int_0^\infty |\psi(x,t)|^2 dx$$
$$= |t_q(v)|^2 = \frac{v^2}{v^2+q^2} = \frac{1}{1+\alpha^2}. \qquad (15)$$

This analysis illustrates that in the high-energy regime the transmission is determined solely by the ratio $\alpha = q/v$, and we predict the dashed (gray) curves of constant transmission which take the form

$$v = \left(\frac{T_q^s}{1-T_q^s}\right)^{1/2} q. \qquad (16)$$

Here we have adopted Holmer's T_q^s notation to denote the limiting case of a high-energy mean-field soliton colliding with a δ-function barrier. In Fig. 1 we display the curves for $T_q^s = 0.1, 0.2, \ldots, 1.0$. It should be noted that these curves are also the transmission rates of plane waves though a δ-function barrier in the linear Schrödinger equation, where the energy is expressed in terms of the velocity instead of the wave number.

Comparing the two sets of curves, we see that the system does, indeed, retrieve a more linear behavior in the high-energy regime where the effect of kinetic energy is greater than that of the nonlinear energy. While the curves do not quantitatively align in the range displayed, they at least share a qualitative agreement. At lower energies, where we see bunching or convergence of the red isocurves which illustrates disallowed states, the transmission behavior departs from being comparable to the linear system and becomes truly nonlinear.

In Fig. 1(b) we display curves of transmission as a function of velocity for a range of values of q. The shaded (red) region is the region of T_+, v combinations disallowed under inequality Eq. (14). In the high-kinetic-energy regime, these curves increase monotonically, but at low kinetic energies this ceases to be true [32–34,41]. We see that here (in the absence of an axial harmonic trap) the disallowed region is quite strict, with no substantial violation of Eq. (14). Indeed, Eq. (14) is generally found to be more strict than the numerical result, as seen by the empty gaps between the disallowed region and the transmission curves.

In Fig. 1(c), the last part that pertains to the axially untrapped case, we display curves of transmission as a function of barrier strength for a range of initial (and thus collisional) velocities. The labeled (red) curve, for which $v = 0.25$, shows the bound below which there is never enough kinetic energy to access all splitting events. We see that all curves $T_+(q;v)$ are discontinuous for $v \leqslant 0.25$, although the discontinuous region is narrower for higher v and is instantaneous for the $v = 0.25$ case.

Figures 1(d)–1(f) are the harmonically trapped counterparts of the figures described above, as we described at the beginning of this section. The behavior is broadly the same; however, there are some specific qualitative and quantitative differences.

In terms of qualitative differences, we see in Figs. 1(e) and 1(f) that there exists a class of solution which appears to access disallowed outcomes, shown by points lying within the shaded (red) region of the plot. Upon closer inspection we determined these outcomes to be bound-state solutions [32]. The energetic arguments leading to Eq. (14) suppose that the solitons are, after splitting, well separated. If this is not the case, then we can access a bound-state solution. In this event, the kinetic-energy shortfall (the deficit of energy required to fully split the soliton) is made up for by the bound-state interaction energy which is gained from the overlap, and attraction, between the resulting solitons. This effect can be greatly enhanced in the harmonically trapped system, where an insufficient kinetic energy after splitting means that the solitons cannot fully separate in the trap, necessitating a bound state.

Quantitatively, we see that the value of v_0 (the velocity of the soliton at the bottom of the trap in the absence of a splitting potential, which we take to be the collisional velocity) must be slightly higher than its untrapped counterpart v in order to access a continuous range of splitting outcomes. This is because the soliton begins to interact with the barrier slightly before it reaches the bottom of the trap at $x = 0$, and so the collisional velocity is, in fact, slightly lower than v_0. This is shown by the gap between the transmission curves and the disallowed region being wider in Fig. 1(e) than in Fig. 1(b) and the labeled (red) transmission curve in Fig. 1(f) having a substantially wider discontinuous region than its counterpart in Fig. 1(c), where the GPE limit of $N \to \infty$ is taken.

D. Classical indicators of the transition to the quantum regime

The behavior we observe here, which describes an energy bound below which the possibility for splitting to occur is progressively curtailed, mirrors behavior which leads to the generation of entangled states [47] in the purely quantum mechanical treatment. Indeed, it has been shown that entangled states in the fully quantum mechanical imply the discontinuities we see here [41]. There is also evidence for the reverse implication [47], and so it is conceivable that these behaviors are equivalent to the extent that transmission discontinuities in the mean-field treatment delimit the regime where mesoscopic Bell states would exist in the fully quantum mechanical treatment, despite these states not being present in the GPE formalism.

E. Analysis of the effect of quantum uncertainty

We now address this high- to low-energy transitional regime by considering how quantum uncertainty impacts the dynamics of the system. The transmission through the barrier is determined by the velocity of the soliton at the point of collision. In the harmonically trapped system, fluctuations in the initial center-of-mass (c.m.) position and momentum will affect this velocity and so affect the transmission. We consider these uncertainties in the harmonically trapped system only, which presents a better defined situation than the untrapped, periodic regime when considering quantum fluctuations of the c.m. In order to delimit a regime where the position and momentum uncertainty of the soliton affects the outcome of a splitting event, we must develop a formalism which allows us to introduce this uncertainty into our system.

First we consider a full many-body treatment of our 1D N-particle system. We can write the first quantized form of the Hamiltonian as [48]

$$\hat{H}(\vec{x}) = \sum_{k=1}^{N}\left(-\frac{\hbar^2}{2m}\frac{\partial^2}{\partial x_k^2} + \frac{m\omega_{\mathrm{T}}^2 x_k^2}{2}\right) - g\sum_{k=2}^{N}\sum_{j=1}^{k-1}\delta(x_k - x_j). \tag{17}$$

In this notation, $\vec{x}$ denotes the vector of the positions of all N particles, $\{x_1, x_2, \ldots, x_N\}$, and all quantities are expressed in their fully dimensional form.

Moving to Jacobi coordinates we can show that the c.m. dynamics and the internal degrees of freedom separate [46] by expressing the Hamiltonian as $H = H_{\mathrm{C}} + H_{\mathrm{R}}$, where

$$H_{\mathrm{C}}(x_{\mathrm{C}}) = -\frac{\hbar^2}{2Nm}\frac{\partial^2}{\partial x_{\mathrm{C}}^2} + \frac{Nm\omega_{\mathrm{T}}^2 x_{\mathrm{C}}^2}{2} \tag{18}$$

is simply the single-particle Hamiltonian for a particle of mass Nm at position x_{C}: the c.m. coordinate. H_{R} describes the residual internal dynamics.

The dimensional wave function for the c.m., ψ_{C}, is then given by

$$\psi_{\mathrm{C}}(x_{\mathrm{C}}) = \left(\frac{1}{\tilde{s}_x\sqrt{2\pi}}\right)^{1/2}\exp\left(-\frac{x_{\mathrm{C}}^2}{4\tilde{s}_x^2}\right), \tag{19}$$

which is simply the 1D wave function of a single particle of mass mN in an axial harmonic trap of frequency ω_{T} normalized to 1. We can interpret $|\psi_{\mathrm{C}}|^2$ as the probability density function for the normally distributed random variable x_{C} such that the expected value is $\langle x_{\mathrm{C}}\rangle = 0$ and the variance (or the position uncertainty of our soliton) is given by $\langle x_{\mathrm{C}}^2\rangle = \tilde{s_x}^2 = 2mN\omega_{\mathrm{T}}/\hbar$.

For our purposes, it is better to consider velocity uncertainty than it is to consider momentum uncertainty. Regardless, we must express our c.m. wave function in momentum space to obtain the momentum/velocity uncertainty. We now use standard result for the Fourier transform of a Gaussian, giving us the Fourier space wave function

$$\phi_{\mathrm{C}}(k_{\mathrm{C}}) = \left(\frac{1}{\tilde{s}_k\sqrt{2\pi}}\right)^{1/2}\exp\left(-\frac{k_{\mathrm{C}}^2}{4\tilde{s}_k^2}\right), \tag{20}$$

where the wave-number variance is $\langle k_{\mathrm{C}}^2\rangle = \tilde{s}_k^2 = 1/4\tilde{s}_x^2 = mN\omega_{\mathrm{T}}/2\hbar$. We can now determine the momentum uncertainty ($\hbar s_k$) and so the velocity uncertainty $\tilde{s}_v = (\hbar/mN)\tilde{s}_k$.

Rescaling the position and velocity uncertainties into dimensionless quantities, we now have

$$s_x = (1/2N\omega_x)^{1/2}, \quad s_v = (\omega_x/2N)^{1/2}. \tag{21}$$

These uncertainties are consistent with the GPE formalism in that as $N \to \infty$ they both disappear. In this limit, the full wave function ψ gives the actual density profile, rather than a probability density function. As such, the c.m. and velocity distribution can be exactly determined.

We now consider this system with an initial condition described by a ground-state soliton at position x_0. If we consider a single observation of the quantum system, we see that the soliton's initial position and velocity are given by $x_0 + x_{\mathrm{f}}$ and v_{f}, where x_{f} and v_{f} denote the quantum fluctuations and are, therefore, normally distributed random variables with mean 0 and standard deviations s_x and s_v, respectively. By classically evolving these initial conditions [according to Eq. (5)] we can apply previous results to state that the final transmission will depend on the fluctuating collisional velocity v_{b}, where $v_{\mathrm{b}} = [\omega_x^2(x_0 + x_{\mathrm{f}})^2 + v_{\mathrm{f}}^2]^{1/2}$.

By rewriting this velocity as $v_{\mathrm{b}} = [\omega_{\mathrm{f}}^2 + v_{\mathrm{f}}^2]^{1/2}$, where $\omega_{\mathrm{f}} = \omega_x(x_0 + x_{\mathrm{f}})$, we can see that v_{b} is essentially the length of a vector composed of two normally distributed random variables: $\omega_{\mathrm{f}} \sim N(\omega_x x_0, s_v^2)$ and $v_{\mathrm{f}} \sim N(0, s_v^2)$. Note that both variables are Gaussian and have the same variance. As such, we can treat the collisional velocity v_{b} as a Rician distributed random variable $v_{\mathrm{b}} \sim R(\omega_x x_0, s_v)$, and so is described (in terms of the Laguerre polynomials of order 1/2, $L_{1/2}$) by mean and variance $\mu_{v_{\mathrm{b}}}, \sigma_{v_{\mathrm{b}}}$ defined as

$$\mu_{v_{\mathrm{b}}} = \mathrm{E}[v_{\mathrm{b}}] = s_v\sqrt{\frac{\pi}{2}}L_{1/2}\left[\frac{-(\omega_x x_0)^2}{2s_v^2}\right], \tag{22}$$

$$\sigma_{v_{\mathrm{b}}}^2 = \mathrm{Var}[v_{\mathrm{b}}] = 2s_v^2 + (\omega_x x_0)^2 - \mu_{v_{\mathrm{b}}}^2. \tag{23}$$

F. Numerical analysis of the effects of quantum uncertainties

1. Overview of the method

We now wish to characterize the effect of c.m. and collision velocity uncertainties on the soliton's transmission through the barrier after being accelerated by the harmonic trap (T_+). To determine the effect of these quantum fluctuations we perform a Monte Carlo analysis, where we numerically evolve the GPE [Eq. (5)] with fluctuations in the initial c.m. position and momentum. This procedure uses the c.m. truncated Wigner approximation (TWA), as used in Ref. [47], to describe the behavior of mesoscopic quantum superpositions. The c.m. TWA was shown to agree well with the effective potential approach of Ref. [20], demonstrating the validity of this method for describing quantum fluctuations in bright soliton systems. Note the related work investigating bright solitons using the TWA in Refs. [23,49].

To characterize the effects of quantum fluctuations, we performed numerical calculations of soliton splitting for varying particle numbers and trap frequencies. We perform these calculations over the same range of velocities as that explored in Sec. III C, allowing for comparisons over the same energetic regime.

Given that this is the velocity range of interest we must select a range of values for the particle number N such that the relevant uncertainties [Eq. (21)] generate fluctuations which are significant relative to the grid spacing in the numerical algorithm. With 4096 spatial grid points over a $-20\pi < x < 20\pi$ domain we have a grid spacing $\Delta x \approx 0.031$. If we now require that $s_x/\Delta x > 10$ (giving 20 grid points within one standard deviation of the spatial mean), we are limited to $N \lesssim 166$. We will distribute N logarithmically over this range (taking powers of 2) and so we consider $N = 16, 32, 64, 128$.

It should be noted that this limit on N was determined with $v_0 = 1$, and so in general there are significantly more than 20 grid points within one standard deviation of the mean. For example, with $N = 16$ and $v_0 = 0.1$ there are more than 200 grid points within one standard deviation of the mean.

In both sections, for each value of v_0 a value of the barrier strength q was selected such that the soliton would be split equally in the absence of quantum fluctuations on the initial condition. The barrier's width was $\sigma_b = 0.2$ for all runs.

2. Transmission sensitivity to quantum fluctuations

We first characterize the sensitivity of the equal splitting case to extreme quantum fluctuations over a continuous range of v_0. For v_0 in the range $0 < v_0 \leqslant 1$ the barrier strength q was found such that $T_+(v_0) = 1/2$. The simulation was then run twice more, replacing the initial position x_0 with $x_\pm = (\mu_{v_{\mathrm{b}}} \pm 3\sigma_{v_{\mathrm{b}}})/\omega_x$ [Figs. 2(a) and 2(b)]. This selection achieves collisional velocities at the barrier of $\mu_{v_{\mathrm{b}}} \pm 3\sigma_{v_{\mathrm{b}}}$. The transmissions associated with these initial conditions [$T_+(\mu_{v_{\mathrm{b}}} \pm 3\sigma_{v_{\mathrm{b}}})$] illustrate the effects of extreme quantum fluctuations. These velocities represent extreme cases of quantum uncertainties adding (removing) energy from the system, and so the $+(-)$ case corresponds to extreme positive (negative) energy quantum fluctuations in the system and will be referred to as such hereafter.

We have also constructed the number fluctuation measure,

$$T_{6\sigma_{v_{\mathrm{b}}}} = \left|T_+\left(\mu_{v_{\mathrm{b}}} + 3\sigma_{v_{\mathrm{b}}}\right) - T_+\left(\mu_{v_{\mathrm{b}}} - 3\sigma_{v_{\mathrm{b}}}\right)\right|. \tag{24}$$

This measure takes values between 0 and 1, with 0 indicating absolute insensitivity to fluctuation and 1 indicating a complete population shift resulting from extreme fluctuations in the initial c.m. position and momentum.

Figure 2(a) shows that $T_+(\mu_{v_{\mathrm{b}}} + 3\sigma_{v_{\mathrm{b}}})$ behaves as we might expect. As the collisional kinetic energy of the system decreases (shown by decreasing v_0), we see that extreme fluctuations in the initial c.m. position and momentum cause a deviation from from equal splitting. At first, when v_0 is relatively high ($v_0 \gtrsim 0.5$), the deviation of T_+ from 0.5 is weakly dependent on v_0. Then, as v_0 approaches 0.25 the effect of disallowed states becomes dominant. In this regime we see that extreme positive-energy quantum fluctuations rapidly enhance transmission.

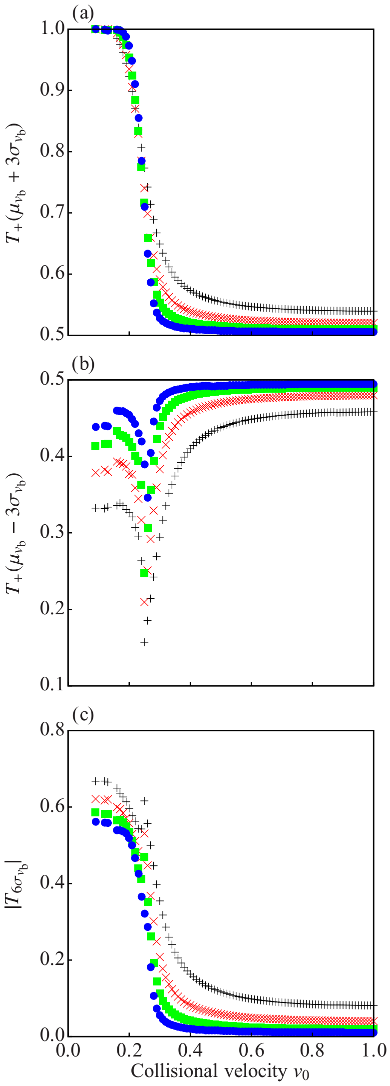

FIG. 2. (Color online) Results of numerical integrations of the GPE illustrating the sensitivity of equal splitting to extreme quantum fluctuation for various particle numbers. The transmissions after extreme positive (negative) energy quantum fluctuations are displayed in panel (a) [panel (b)]. The number fluctuation measure $T_{6\sigma_{v_b}}$ [Eq. (24)] is plotted in (c). For all plots we show $N = 16$ (+), 32 (×), 64 (■), and 128 (•).

The effects of extreme negative-energy quantum fluctuations, quantified by $T_+(\mu_{v_b} - 3\sigma_{v_b})$, are slightly more complicated. The careful selection of q makes the bound states (as described in Sec. III B and observed in Sec. III C) a notable factor. This can be seen by the more complex structure of the data displayed in Fig. 2(b). At the high-energy end of the velocity range we see the same weak deviation of T_+ from 0.5 as that described above for extreme positive-energy fluctuations. However, where we might expect disallowed states to enhance reflection (namely $v \lesssim 0.25$), we see a revival in the transmission. This is a result of a bound state confining the wave function to the region around the barrier at the bottom of the trap, resulting in a T_+ failing to tend to 0. This effect is consistent with the reduced kinetic energy being insufficient to split the soliton in the low-velocity regime.

Finally, in Fig. 2(c) we see that $T_{6\sigma_{v_b}}$ does generally increase as v_0 decreases, showing that number fluctuations become very important at low kinetic energies as a result of energetically disallowed states enhancing transmission and/or reflection. However, as a result of the previously discussed impact of bound states, $T_{6\sigma_{v_b}}$ does not vary smoothly between 0 and 1. This effect could be treated as an artifact and removed by only taking the post splitting positive domain integral (T_+) far from the barrier, thus excluding bound states. This would give a continuous, smooth range between 0 and 1 but would obscure the effect of bound states.

3. Monte Carlo analysis of transmission with quantum fluctuations

In order to characterize the distribution of the transmission T_+ after factoring in quantum uncertainty in the initial condition we performed a selection of Monte Carlo simulations. These simulations allow us to develop a broader qualitative understanding of the effects of quantum uncertainty. Here we have selected the same values of the particle number N as used previously and consider velocities $v_0 = 0.3, 0.5, 0.7, 0.9$. We present the results of 1000 Monte Carlo simulations for each v_0, N pair.

Figure 3 displays the different distributions of the transmission T_+ which arise from varying the energetic regime and particle number. In the bottom row we see that for high v_0 the distribution is a narrow Gaussian for all displayed N. Reducing v_0 for a given N (reading up the column) causes the standard deviations of the Gaussians to broaden. For $v_0 = 0.3$ (the top row of Fig. 3) a bimodal distribution appears, again illustrating that the equal splitting case is less easily accessed. This behavior is evident for all N. Reading across the rows (varying N while keeping v_0 constant) shows that increasing N simply reduces the width of the transmission distribution. This illustrates that the N dependence is secondary to the v_0 dependence in the range explored here. This is evident in that there is still significant broadening of the transmission distribution at low v_0 even for the highest values of N. We might expect this to be the case, given that the range of N explored here is, in experimental terms, very low.

We can see the functional dependence of transmission on v_b [$T_+(v_b)$] in Fig. 4. We see that in the higher energetic regime ($v_0 > 0.5$) the transmission has a weak approximately linear dependence on the velocity. The relatively small gradient of this dependence indicates that the transmission is less sensitive to the fluctuations. For the $v_0 = 0.3$ data we see that the dependence becomes very sensitive to small fluctuations around $v_b = 0.3$, the equal splitting case. This confirms that proximity to the energetically disallowed state can cause large variations in transmission when quantum fluctuations are considered. Increasing N has the effect of narrowing the distributions of the fluctuations, and so these fluctuations can affect the transmission less dramatically, even when close to the energetically disallowed state. It should be noted that the points in Fig. 4 lie along curves with structure analogous to those depicted in Fig. 1(e).

We can quantify the relationship between the initial quantum uncertainties (via σ_{v_b}) and the resulting transmission uncertainty σ_{T_+} by making a maximum likelihood estimate $\bar{s}_{T_+}$

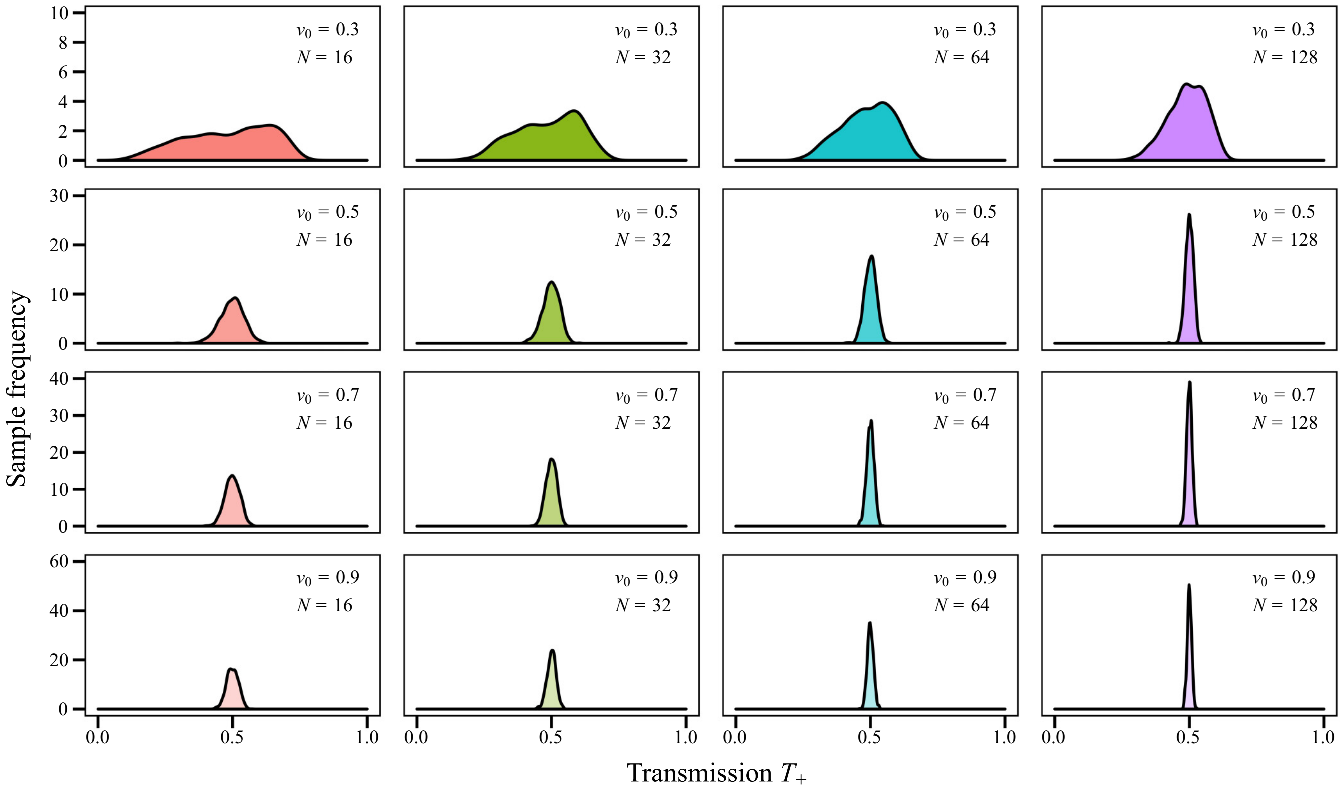

FIG. 3. (Color online) Distributions of the transmission T_+ obtained from Monte Carlo simulations. Here we show results for a range of trap frequencies and particle numbers, giving a range of uncertainties in the initial c.m. position and momentum. In the range explored, we see that the effects of varying the trap frequency (and so kinetic energy) dominate the dynamics, with narrow Gaussians at high energy, but a bimodal structure arising at low energy when energetically disallowed states arise.

based on our data. We assume that the data follows a truncated Gaussian distribution on the interval [0,1]. The results of these estimates are shown in Fig. 5. We see that $\bar{s}_{T_+}$ has approximately linear correlations with σ_{v_b}. This correlation becomes stronger, illustrated by the increased gradient of the linear fit, as we reduce v_0. The gray shaded areas indicate a 95% confidence interval for the least-squares linear regression. The confidence interval associated with $v_0 = 0.3$ is widest, indicating a less linear relation between σ_{v_b} and $\bar{s}_{T_+}$ in the low-energy regime.

G. Split-induced phase shift

In order to construct an analysis of soliton interferometry there is another aspect of soliton splitting which we must address. The act of splitting the soliton (which gives us two coherent matter waves to interfere) causes a phase difference to arise between the solitons. This is similar to the case of classical optics. A classical analysis of electromagnetic fields at interfaces between media, yielding the Fresnel equations [50], shows us that when light passes into a medium with a higher refractive index the reflected part is phase shifted by π with respect to the transmitted part. This effect is particularly relevant in the case of optical interferometers where a beam of light is split by a beam splitter. In the case of soliton splitting the principle is similar, and the barrier (here acting as our beam splitter) imparts a phase difference between the two residual solitons. In contrast to the optical case, the transmitted soliton is $\pi/2$ phase shifted with respect to the reflected soliton. In other words, the phase difference has half the magnitude and opposite sign. This difference between the two cases is understandable because the two are very different physical systems and so are governed by very different sets of equations. The systems are analogous but, of course, not identical. We now present a derivation of this phase shift.

It has been rigorously analytically shown [30] that, in the high-kinetic-energy limit (high soliton velocity v) of the 1D untrapped system, when a soliton is split at a δ-function barrier the phases imparted to the solitons by the split are

$$\begin{aligned}\vartheta_T &= \left[1 - A_T^2\right]\left|\frac{x_0}{2v}\right| + \arg[t_q(v)] + \vartheta_0(|t_q(+v)|),\\ \vartheta_R &= \left[1 - A_R^2\right]\left|\frac{x_0}{2v}\right| + \arg[r_q(v)] + \vartheta_0(|r_q(-v)|),\end{aligned} \tag{25}$$

where $\vartheta_{R,T}$ are the reflected, transmitted soliton phases and $A_{R,T}$ are the reflected, transmitted soliton amplitudes. Quantities $r_q(v)$ and $t_q(v)$ are the transmission and reflection rates of a δ function in the linear regime, given by

$$t_q(v) = \frac{iv}{iv - q} \quad \text{and} \quad r_q(v) = \frac{q}{iv - q}. \tag{26}$$

If the barrier strength and initial velocity (q and v) are selected to be equal ($q = v$), such that $|r_q(v)| = |t_q(v)|$ and (as a result)

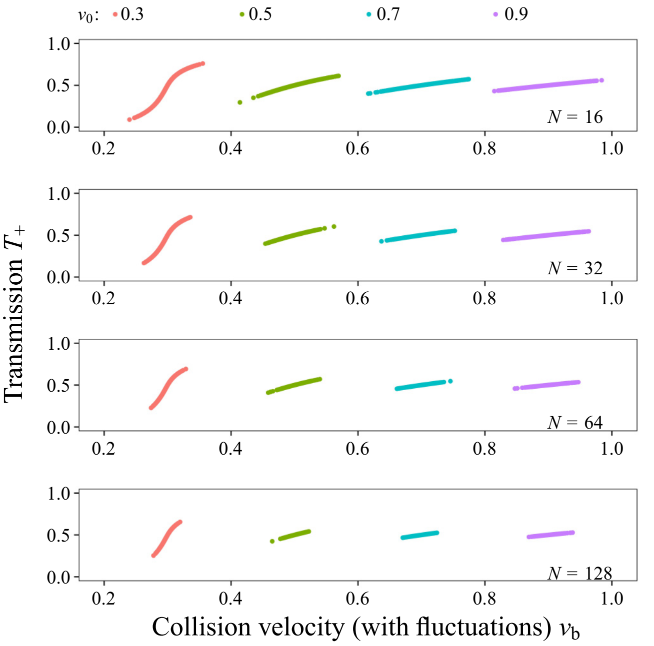

FIG. 4. (Color online) Results of Monte Carlo simulations. Here we show the dependence of transmission on T_+ on the collision velocity (v_b) after quantum position and momentum fluctuations have been added to a base collision velocity (v_0). For each v_0 the barrier strength was set to ensure equal splitting in the limit of zero fluctuations. We see that in the low-energy regimes the transmission can be very sensitive to quantum fluctuations.

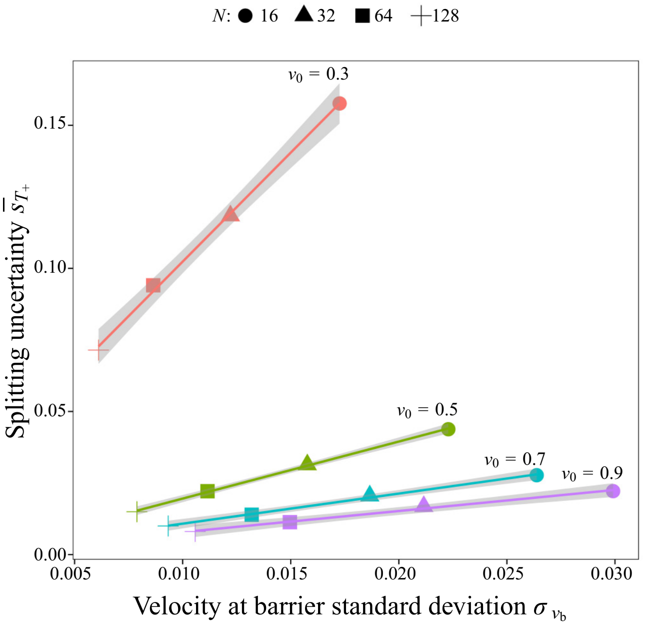

FIG. 5. (Color online) Results of Monte Carlo simulations. Shown here are the standard deviations associated with the final transmission distributions depicted in Fig. 3. We see a weak linear dependence on the sample velocity uncertainty $\bar{s}_{v_\mathrm{b}}$ for high v_0, which becomes stronger, but less linear, as we reduce the energy. This can be seen by the widening (shaded) 95% confidence intervals of the linear fits.

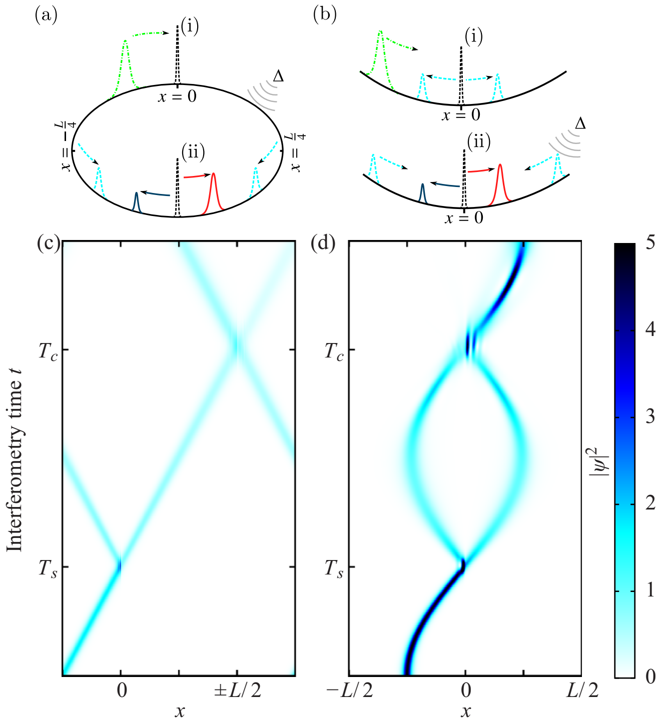

FIG. 6. (Color online) (a) Diagram of a Mach-Zehnder interferometer utilizing a periodic confinement with two antipodal barriers. An example of the time evolution of the density for this configuration is displayed in (c). (b) Diagram of a Mach-Zehnder interferometer utilizing harmonic confinement and a single splitting barrier. Again, an example of the time evolution for such a configuration is displayed in (d).

$A_R = A_T$ then the soliton is split equally into two secondary solitons of equal amplitude. This is desirable because later we will wish to collide the resulting solitons at a barrier, and if these solitons are of similar size then the interference between them is more pronounced. It is also true that a size difference causes secondary nonlinear phase shifts to arise during the collision, which is undesirable.

Making this selection, such that the soliton is equally split, and substituting appropriate values of q, v, $A_{R,T}$, $|r_q(v)|$, and $|t_q(v)|$ into Eq. (25), we see that the relative phase between the solitons reduces to

$$\vartheta_T - \vartheta_R = \arg[t_q(v)] - \arg[r_q(v)] = \pi/2. \qquad (27)$$

A broader discussion of the effect of a finite-width barrier on the phase shift accumulated during splitting is, again, available in Ref. [32]. We use the $\pi/2$ figure as an estimate of the phase difference accumulated by splitting on a Gaussian barrier, as justified in Ref. [18], for the rest of the current work.

IV. SOLITON INTERFEROMETRY

A. Analysis of soliton interferometry

We can use the above results regarding soliton interactions at narrow barriers to analyze and construct a soliton interferometer. Soliton interferometry is a three step process.

First we split a ground-state soliton into two lesser solitons of equal size at a narrow potential barrier [Figs. 6(a) and 6(b) (i)]. In the case of a δ-function barrier, this split causes the transmitted soliton to gain a $\pi/2$ phase shift relative to the reflected soliton, as described in Sec. III G.

These solitons then accumulate a further relative phase difference δ_{MZ}. This phase difference is the quantity we wish to measure. In the current work we consider the case where this difference is gained by exposing one soliton to a phase-shifting phenomenon.

In the third step the two solitons are made to collide at a narrow barrier [Figs. 6(a) and 6(b) (ii)]. After this final barrier collision the wave-function integrals on either side of the barrier,

$$I_{\pm} = \pm \int_0^{\pm\infty} |\psi(x)|^2 dx, \tag{28}$$

allow us to determine the magnitude of δ_{MZ} [Figs. 6(a) and 6(b) (ii)]. Here I_+ is the positive domain population and I_- is the negative domain population. We can determine the dependence of $I_\pm$ on δ_{MZ} by recalling previous work by the authors [18] in which it was shown that after two initially distinct solitons collide at a barrier, and had relative phase Δ before the collision, the populations in the negative and positive domains,

$$T_{\pm} = \pm \lim_{t\to\infty} \int_0^{\pm\infty} |\psi(x,t)|^2 dx, \tag{29}$$

are given by

$$T_{\pm} = \frac{1 \pm \sin(\Delta + \epsilon)}{2}, \tag{30}$$

where

$$\lim_{v\to\infty} \max(|\epsilon|) = 0. \tag{31}$$

Using this result we can see that taking the phase difference Δ to be the sum of the phase shift we wish to measure, δ_{MZ}, and the phase shift accumulated during the initial split, $\pi/2$ we obtain

$$I_{\pm} = \frac{1 \pm \cos(\Delta + \epsilon)}{2}. \tag{32}$$

The different types of soliton interferometry available are determined by the geometry of the potentials used to confine and split the BEC. Here we investigate two different geometries. The first is a toroidal trap giving a periodic geometry with two splitting potentials at antipodal points (Sec. IV B) [Figs. 6(a) and 6(c)]. This geometry is somewhat challenging to create experimentally but provides the simplest framework in which to establish our analytical results. The second geometry uses a nonperiodic geometry with a weak axial harmonic trap centered on a narrow splitting potential (Sec. IV C) [Figs. 6(b) and 6(d)]. This geometry makes is more experimentally viable, but questions of broken integrability require that we confirm the applicability of the results established above.

We now present more expansive numerical analyses of these cases in order to determine whether our analytical results are confirmed numerically and also to determine the best energy regime in which to attempt soliton interferometry.

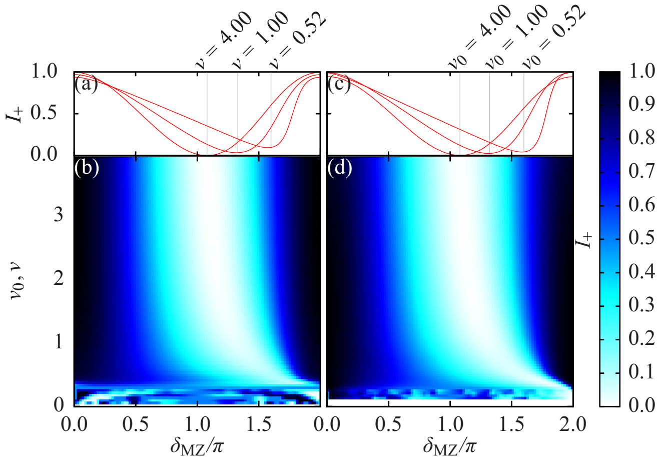

FIG. 7. (Color online) Numerically calculated transmission rates after the second collision, I_+, for two Mach-Zehnder interferometry geometries. Color maps for the (b) toroidal Mach-Zehnder and (d) harmonic Mach-Zehnder cases show the full parameter space. Panels (a) and (c) show specific curves of constant v, v_0 for the same respective scenarios and highlight the transition from the high-energy sinusoidal dependence regime to the lower-energy quasilinear dependence regime.

B. Toroidal confinement Mach-Zehnder interferometry

An often discussed trapping geometry is the periodic toroidal trap. The existence of experimental results utilizing optical [45] and magnetic [51,52] confinement methods coupled with theoretical investigations proving localized bright soliton states exist in the truncated mean-field Hamiltonian [53], 3D GPE [54], and coupled Gross-Pitaevskii Bogoliubov–de Gennes equations [55,56] makes it worthwhile to consider extending our theory into this geometry. The toroidal geometry is beneficial in that it has no axial trapping, the presence of which breaks integrability and could, arguably, compromise our previous results.[3]

By treating Eq. (5) as periodic over the domain $-L/2 < x \leqslant L/2$, such that $\psi(-L/2) = \psi(L/2)$, we obtain a suitable dynamics equation. We use the same initial condition [Eq. (8)] and initial offset, but set the trap frequency $\omega_x = 0$ and directly vary the velocity v by imprinting a phase on the initial condition.

Results of GPE simulations are shown in Figs. 7(a) and 7(b). We see that for very high velocities, $v \approx 4$, the interference follows our prediction [Eq. (32)] closely, with very small skews arising from nonlinear effects during the final barrier collision, showing that $\epsilon \approx 0$ in this regime.

As the velocity decreases, and we enter the transitional regime between high and low kinetic energy, ϵ increases and the skew becomes more prominent. As this happens the interference curve ceases to be sinusoidal and becomes approximately linear over some range, with $I_\pm \propto \mp\delta_{\mathrm{MZ}}$ up

---

[3] Indeed, adding any potential breaks the integrability, but for narrow splitting barriers one can consider the system to be widely integrable with small regions where the solution behaves differently.

to some discontinuity. This discontinuity becomes narrower for higher ϵ and is situated at 2π for $v \approx 0.3$. In this regime, however, we are drawing close to the regime where equal soliton splitting becomes disallowed. For $v \lesssim 0.3$ the structure of the transmission becomes very complex, as the sensitivity of splitting to small changes in velocity becomes apparent. In this regime, soliton interferometry becomes impracticable.

C. Harmonic confinement Mach-Zehnder interferometry

1. Overview

When considering trapping geometries for BEC experiments it is important to note that the addition of an axial harmonic trap globally breaks the integrability of the system, and so we can no longer say that we are studying true NLSE solitons in the mathematical sense. It is true, however, that the bright solitary waves supported by the system and confined in the harmonic trapping potential behave in a very solitonlike manner, staying robust to collisions and retaining their forms for long periods. Investigations utilizing particle Hamiltonian models [9] to describe the soliton motion agree well with GPE simulations, and so we can safely treat these bright solitary waves as solitons.

2. Classical numerical analysis

The results of fully classical numerical simulations are displayed in Figs. 7(c) and 7(d), obtained by evolving the initial condition described by Eq. (8) according to Eq. (5). In this case, the initial velocity v was set to zero while the soliton's velocity at the barrier, v_0, was set by varying the axial trap frequency ω_x (The dimensionless from of $\omega_{\rm T}$) and holding the initial offset x_0 at a constant value such that the soliton is initially well separated from the barrier.

The results are comparable to those seen for the periodic Mach-Zehnder case (Sec. IV B), with good agreement with theory for high velocities, a linear dependence arising as we approach $v_0 \approx 0.3$ and finally complex structure arising in the low-energy regime making interferometry impracticable.[4]

3. Interferometry sensitivity to quantum fluctuations

It was stated above that the linear relation between final domain population and phase shift might make interferometry more easily interpreted in the lower velocity regime. However, if we are to work in the regime we must consider the implications of the results outlined in Sec. III, namely the impacts of energetically disallowed states and quantum uncertainty in the initial condition.

We again characterize the system's sensitivity to extreme positive and negative-energy fluctuations. As such, we construct the quantities $I_+(\mu_{v_{\rm b}} \pm 3\sigma_{v_{\rm b}})$ and

$$I_{6\sigma_{v_{\rm b}}} = \left| I_+\left(\mu_{v_{\rm b}} + 3\sigma_{v_{\rm b}}\right) - I_+\left(\mu_{v_{\rm b}} - 3\sigma_{v_{\rm b}}\right)\right|. \tag{33}$$

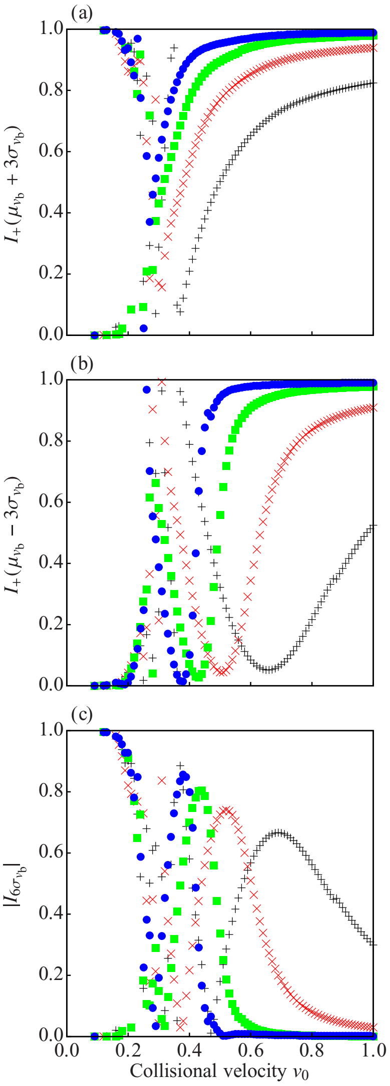

FIG. 8. (Color online) Results of numerical integrations illustrating the sensitivity of interferometry to extreme quantum fluctuation for various particle numbers. The interferometry transmissions after extreme positive (negative)-energy quantum fluctuations are displayed in panel (a) [panel (b)]. The number fluctuation measure $I_{6\sigma_{v_{\rm b}}}$ [Eq. (33)] is plotted in (c). For all plots we show $N = 16$ (+), 32 (×), 64 (■), and 128 (●).

These quantities are analogous to those used previously (Sec. III F 2), but are obtained by allowing the system to evolve through the entire process of interferometry, rather than just the initial splitting event. In this section and the next section [where we discuss results displayed in 8, 9, 10, and 11] we have considered the $\Delta = 0$ case only in order to simplify our analysis.

Figure 8 shows the results of these simulations. We see that for high N and high v_0 the systems are reasonably insensitive to fluctuations. However, even in the high-energy limit we see that as we decrease N the interferometry transmissions significantly deviate from their asymptotic values. This sensitivity is high compared to that of the single splitting case, illustrating that the process of splitting (which occurs twice in interferometry) enhances the sensitivity of the classical system

---

[4] It should be noted that in the data set displayed in Fig. 7(d) is incomplete. The solid white band at $v \approx 0$ is a region where the system evolved too slowly to be numerically practical.

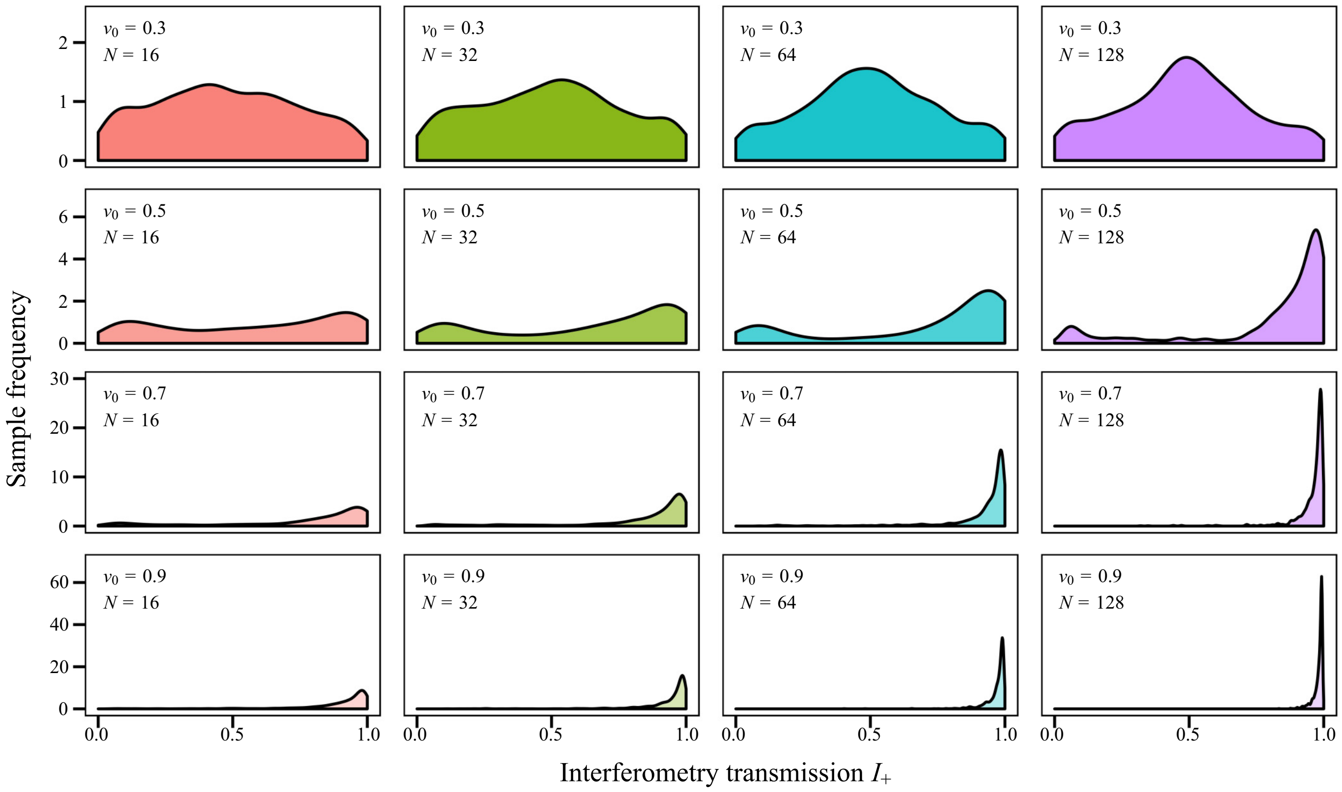

FIG. 9. (Color online) Distributions of the interferometry transmission I_+ obtained from Monte Carlo simulations. Here we show results for a range of trap frequencies and particle numbers, giving a range of uncertainties in the initial c.m. position and momentum. In the range explored, we see that the effects of varying the trap frequency (and so kinetic energy) dominate the dynamics, with narrow Gaussians at high energy, but a uniform structure arising at low energy when interferometry becomes impracticable.

to initial fluctuations. The double enhancement in interferometry requires that we must be closer to the mean-field limit or suffer intolerable deviations from the classical behavior.

As we decrease v_0 still further the previously discussed bound states and disallowed splitting events greatly complicate the dynamics of interferometry, making both the system and the results of our numerics difficult to interpret. This difficulty clearly shows that interferometry is impracticable in the low-energy limit.

4. Monte Carlo analysis of interferometry with quantum fluctuations

We now present a Monte Carlo analysis of the effects of quantum uncertainties in the c.m. initial position and momentum. We explore the same parameter regime as in Sec. III F 3 and again present the results of 1000 Monte Carlo simulations. The histograms in Fig. 9, illustrating the distributions of the interferometry transmission I_+, show characteristics similar to those in Fig. 3, but more pronounced. The distributions are approximately Gaussian at higher energies and particle numbers, but become more uniform at low energies ($v_0 = 0.3$), with a peak in the frequencies near $I_+ = 0.5$ arising from the presence of persistent bound states. This again indicates that interferometry is not viable in the low-energy regime.

The transmission curves in Fig. 10 have a much more complex structure than that exhibited in its counterpart, Fig. 4. At higher velocities, the points are clearly centered on the $I_+ = 1$ state, as we would expect, but as we lower the velocity the transmission becomes very sensitive to quantum fluctuations. This can be attributed to nonlinear phase shifts arising during the soliton collision at the barrier, compounded by a mismatch between the barrier strength and soliton velocity upon collision. Indeed, for the $v_0 = 0.3$ case these nonlinear phase shifts can cause I_+ to take literally any value between 0 and 1, and the quantum fluctuations cause I_+ to tune across this period multiple times. This, alone, precludes any possibility of soliton interferometry in this regime. It is also visible that, even for high energies, a particle number of less than ≈130 can cause increased sensitivity, and so we really must ensure that we are in the regime of high N. After these considerations have been taken into account, it should be possible to perform interferometry with a quasilinear signal [similar to that associated with the $v_0 = 0.52$ curve in Fig. 1(e)] for values of $v_0 \gtrsim 0.5$.

Finally, we again calculated maximum likelihood estimates of the variance $\bar{s}_{I_+}$ of the transmission, which we again assumed to be distributed as a truncated Gaussian. The results of these calculations are displayed in Fig. 11. At higher velocities, we see an approximately linear correlation between the transmission uncertainty and collisional velocity uncertainty standard deviation σ_{v_b}. The gradient of the regression lines is much steeper than those in Fig. 5, showing the increased sensitivity of I_+ to quantum fluctuations. Again, the shaded

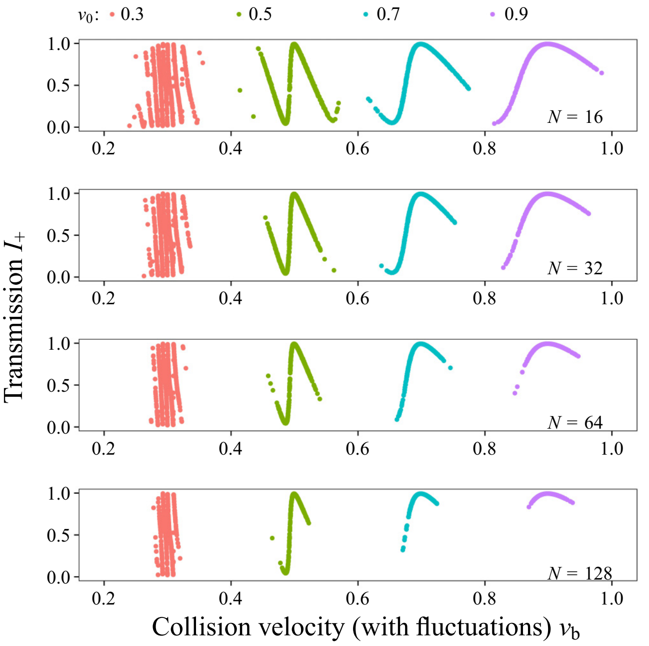

FIG. 10. (Color online) Results of Monte Carlo simulations. Here we show the dependence of interferometry transmission on I_+ on the collision velocity (v_b) after quantum position and momentum fluctuations have been added to a base collision velocity (v_0). For each v_0 the barrier strength was set to ensure equal splitting in the limit of zero fluctuations. We see that in the low-energy regimes the complex and velocity-sensitive structure of the transmission renders interferometry unworkable.

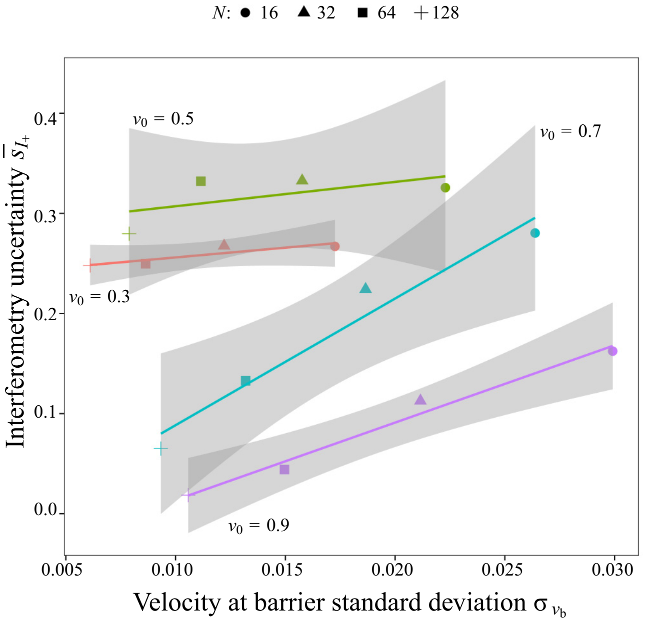

FIG. 11. (Color online) Results of Monte Carlo simulations. Here the standard deviation associated with the final interferometry distributions depicted in Fig. 9. We see a strong, weakly linear dependence on $\bar{s}_{v_b}$ for high v_0, which becomes stronger, but less linear, as we reduce the energy. The variance saturates when the distribution becomes effectively uniform.

regions show a 95% confidence interval for the linear fit. For all velocities shown the confidence intervals are notably wider than their counterparts in Fig. 5, and so we can conclude that the dependence of $\bar{s}_{I_+}$ on σ_{v_b} is more complicated than in the soliton splitting case, as we would expect. At lower velocities $\bar{s}_{I_+}$ saturates below ~0.4. This is a result of attempting to fit a Gaussian to a distribution which is, in effect, uniform. This becomes apparent when we consider that ~38% of the probability mass of a Gaussian lies within a central period of width σ, and so applying a fitting algorithm to a uniform distribution will likely produce a standard deviation with a width encompassing ~38% of the sample. In this case, that width is ~0.4. This saturation is a strong indicator of a velocity and/or particle number regime in which interferometry is unworkable.

V. CONCLUSIONS

We have shown analytic results describing soliton interferometry in the ideal classical case, specifically the case of a toroidal Mach-Zehnder configuration. We have extended these results to the harmonically trapped system, which is currently more experimentally relevant than the toroidal case [4] and presents a better defined situation when considering quantum fluctuations of the c.m. This has allowed us to investigate and delimit the energetic regimes in which quantum fluctuations in the initial c.m. position and momentum cause the classical dynamics to break down.

This low-energy-regime failure of classical results is primarily caused by disallowed soliton splitting events, extremely discontinuous transmission curves, and bound states. These factors complicate the early evolution of the interferometric system and compromise the dynamics. As we approach the low-energy-regime quantum effects mix these phenomena into the dynamics of the system where classically they would be absent. This causes greatly enhanced sensitivity to quantum effects in both the splitting transmission and the interferometry transmission when close to the low-energy regime. This sensitivity appears at marginally higher kinetic energies in the presence of harmonic trapping, but the difference is relatively slight for the weak trapping considered.

We conclude that whether or not the mean-field limit is truly achieved, soliton interferometry is not a viable process in the extremely, or even transitionally, low-kinetic-energy regime. However, for a suitably high initial kinetic energy we see good results for particle numbers upwards of the low hundreds (beyond which our numerical algorithm struggles to resolve fluctuations, also indicating that the classical model is robust in this regime).

ACKNOWLEDGMENTS

We thank S. L. Cornish, A. S. Bradley, T. P. Billam, D. I. H. Holdaway, P. Mason, and A. L. Marchant for useful discussions and the UK EPSRC (Grants No. EP/G056781/1 and No. EP/K03250X/1) and The Royal Society (Grant No. IE110202) for support. S.J.R. is supported by the University of Otago and thanks Durham University for its hospitality.

[1] L. Khaykovich, F. Schreck, G. Ferrari, T. Bourdel, J. Cubizolles, L. D. Carr, Y. Castin, and C. Salomon, Science **296**, 1290 (2002).

[2] K. E. Strecker, G. B. Partridge, A. G. Truscott, and R. G. Hulet, Nature (London) **417**, 150 (2002).

[3] S. L. Cornish, S. T. Thompson, and C. E. Wieman, Phys. Rev. Lett. **96**, 170401 (2006).

[4] A. L. Marchant, T. P. Billam, T. P. Wiles, M. M. H. Yu, S. A. Gardiner, and S. L. Cornish, Nat. Commun. **4**, 1865 (2013).

[5] S. E. Pollack, D. Dries, E. J. Olson, and R. G. Hulet, 2010 DAMOP: Conference abstract, http://meetings.aps.org/link/BAPS.2010.DAMOP.R4.1.

[6] S. A. Morgan, R. J. Ballagh, and K. Burnett, Phys. Rev. A **55**, 4338 (1997).

[7] N. G. Parker, A. M. Martin, C. S. Adams, and S. L. Cornish, Physica D **238**, 1456 (2009).

[8] T. P. Billam, S. L. Cornish, and S. A. Gardiner, Phys. Rev. A **83**, 041602(R) (2011).

[9] A. D. Martin, C. S. Adams, and S. A. Gardiner, Phys. Rev. Lett. **98**, 020402 (2007).

[10] A. D. Martin, C. S. Adams, and S. A. Gardiner, Phys. Rev. A **77**, 013620 (2008).

[11] D. Poletti, T. J. Alexander, E. A. Ostrovskaya, B. Li, and Y. S. Kivshar, Phys. Rev. Lett. **101**, 150403 (2008).

[12] V. E. Zakharov and A. B. Shabat, Zh. Eksp. Teor. Fiz. **61**, 118 (1971) [Sov. Phys. JETP-USSR **34**, 62 (1972)].

[13] J. Satsuma and N. Yajima, Prog. Theor. Phys. Suppl. **55**, 284 (1974).

[14] J. P. Gordon, Opt. Lett. **8**, 596 (1983).

[15] H. A. Haus and W. S. Wong, Rev. Mod. Phys. **68**, 423 (1996).

[16] L. Helczynski, B. Hall, D. Anderson, M. Lisak, A. Berntson, and M. Desaix, Phys. Scr. **2000**, 81 (2000).

[17] T. P. Billam, S. A. Wrathmall, and S. A. Gardiner, Phys. Rev. A **85**, 013627 (2012).

[18] J. L. Helm, T. P. Billam, and S. A. Gardiner, Phys. Rev. A **85**, 053621 (2012).

[19] S. L. Cornish, N. G. Parker, A. M. Martin, T. E. Judd, R. G. Scott, T. M. Fromhold, and C. S. Adams, Physica D **238**, 1299 (2009).

[20] C. Weiss and Y. Castin, Phys. Rev. Lett. **102**, 010403 (2009).

[21] A. I. Streltsov, O. E. Alon, and L. S. Cederbaum, Phys. Rev. A **80**, 043616 (2009).

[22] U. Al Khawaja and H. T. C. Stoof, New J. Phys. **13**, 085003 (2011).

[23] A. D. Martin and J. Ruostekoski, New J. Phys. **14**, 043040 (2012).

[24] T. Fogarty, A. Kiely, S. Campbell, and T. Busch, Phys. Rev. A **87**, 043630 (2013).

[25] J. Cuevas, P. G. Kevrekidis, B. A. Malomed, P. Dyke, and R. G. Hulet, New J. Phys. **15**, 063006 (2013).

[26] Y. S. Kivshar and B. A. Malomed, Rev. Mod. Phys. **61**, 763 (1989).

[27] T. Ernst and J. Brand, Phys. Rev. A **81**, 033614 (2010).

[28] C. Lee and J. Brand, Europhys. Lett. **73**, 321 (2006).

[29] X. D. Cao and B. A. Malomed, Phys. Lett. A **206**, 177 (1995).

[30] J. Holmer, J. Marzuola, and M. Zworski, Commun. Math. Phys. **274**, 187 (2007).

[31] J. Holmer, J. Marzuola, and M. Zworski, J. Nonlin. Sci. **17**, 349 (2007).

[32] J. Polo and V. Ahufinger, Phys. Rev. A **88**, 053628 (2013).

[33] C.-H. Wang, T.-M. Hong, R.-K. Lee, and D.-W. Wang, Opt. Express **20**, 22675 (2012).

[34] S. Damgaard Hansen, N. Nygaard, and K. Mølmer, arXiv:1210.1681.

[35] M. Minmar, Ph.D. thesis, Stanford University, 2012.

[36] W. Królikowski and Y. S. Kivshar, J. Opt. Soc. Am. B **13**, 876 (1996).

[37] A. Fratalocchi and G. Assanto, Phys. Rev. E **73**, 046603 (2006).

[38] V. V. Konotop, D. Cai, M. Salerno, A. R. Bishop, and N. Grønbech-Jensen, Phys. Rev. E **53**, 6476 (1996).

[39] R. G. Hulet, S. Pollack, D. Dries, and E. Olson, *NLQUGAS: Nonlinear Phenomena in Degenerate Quantum Gases: Ourense Spain (conference abstracts)*, edited by J. R. Salgueiro (2010), p. 31.

[40] P. B. Blakie, A. S. Bradley, M. J. Davis, R. J. Ballagh, and C. W. Gardiner, Adv. Phys. **57**, 363 (2008).

[41] B. Gertjerenken, T. P. Billam, L. Khaykovich, and C. Weiss, Phys. Rev. A **86**, 033608 (2012).

[42] C. Pethick and H. Smith, *Bose-Einstein Condensation in Dilute Gases* (Cambridge University Press, Cambridge, UK, 2002).

[43] T. W. Neely, A. S. Bradley, E. C. Samson, S. J. Rooney, E. M. Wright, K. J. H. Law, R. Carretero-González, P. G. Kevrekidis, M. J. Davis, and B. P. Anderson, Phys. Rev. Lett. **111**, 235301 (2013).

[44] C. Ryu, P. W. Blackburn, A. A. Blinova, and M. G. Boshier, Phys. Rev. Lett. **111**, 205301 (2013).

[45] A. Ramanathan, K. C. Wright, S. R. Muniz, M. Zelan, W. T. Hill, C. J. Lobb, K. Helmerson, W. D. Phillips, and G. K. Campbell, Phys. Rev. Lett. **106**, 130401 (2011).

[46] D. I. H. Holdaway, C. Weiss, and S. A. Gardiner, Phys. Rev. A **85**, 053618 (2012).

[47] B. Gertjerenken, T. P. Billam, C. L. Blackley, C. R. Le Sueur, L. Khaykovich, S. L. Cornish, and C. Weiss, Phys. Rev. Lett. **111**, 100406 (2013).

[48] E. H. Lieb and W. Liniger, Phys. Rev. **130**, 1605 (1963).

[49] B. J. Dąbrowska-Wüster, S. Wüster, and M. J. Davis, New J. Phys. **11**, 053017 (2009).

[50] E. Hecht, *Optics*, 4th ed. (Addison Wesley, Boston, 2001).

[51] S. Gupta, K. W. Murch, K. L. Moore, T. P. Purdy, and D. M. Stamper-Kurn, Phys. Rev. Lett. **95**, 143201 (2005).

[52] J. A. Sauer, M. D. Barrett, and M. S. Chapman, Phys. Rev. Lett. **87**, 270401 (2001).

[53] G. M. Kavoulakis, Phys. Rev. A **67**, 011601 (2003).

[54] A. Parola, L. Salasnich, R. Rota, and L. Reatto, Phys. Rev. A **72**, 063612 (2005).

[55] L. Salasnich, A. Parola, and L. Reatto, Phys. Rev. A **74**, 031603 (2006).

[56] L. Salasnich, B. A. Malomed, and F. Toigo, Phys. Rev. A **76**, 063614 (2007).